POLITECNICO DI TORINO
Repository ISTITUZIONALE

Numerical optimization of ejector for enhanced hydrogen recirculation in proton exchange membrane fuel cells

Original
Numerical optimization of ejector for enhanced hydrogen recirculation in proton exchange membrane fuel cells / Arabbeiki, M., Mansourkiaei, M., Ferrero, D., Santarelli, M.. - In: JOURNAL OF POWER SOURCES. - ISSN 0378-7753. - 641:(2025). [10.1016/j.jpowsour.2025.236846]

Availability:
This version is available at: 11583/3014488 since: 2026-08-15T00:41:30Z

Publisher:
Elsevier B.V.

Published
DOI:10.1016/j.jpowsour.2025.236846

Terms of use:

This article is made available under terms and conditions as specified in the corresponding bibliographic description in the repository

Publisher copyright

(Article begins on next page)

20 November 2026

Journal of Power Sources 641 (2025) 236846

Contents lists available at ScienceDirect

Journal of Power Sources

journal homepage: www.elsevier.com/locate/jpowsour

Numerical optimization of ejector for enhanced hydrogen recirculation in proton exchange membrane fuel cells

Masoud Arabbeiki, Mohsen Mansourkiaei, Domenico Ferrero *, Massimo Santarelli

Department of Energy (DENERG), Politecnico di Torino, 10129, Turin, Italy

HIGHLIGHTS

- CFD and Box-Behnken design used for PEMFC ejector optimization.
- NSGA-II and desirability function improved ejector's entrainment ratio.
- Choked flow maintained in ejector under both design and off-design conditions.
- Key geometric parameters significantly impact ejector performance.
- Optimized ejector geometry enhances PEMFC hydrogen recirculation by 20 %.

ARTICLE INFO

Keywords:
Proton exchange membrane fuel cell
Ejector
Hydrogen recirculation
Multi-objective optimization
Box-Behnken design

ABSTRACT

In proton exchange membrane fuel cell (PEMFC) systems, ejectors enable hydrogen recirculation without parasitic power consumption. However, their performance is highly sensitive to design parameters and operating conditions, often leading to inefficiencies under off-design conditions. This study develops a comprehensive numerical optimization framework integrating computational fluid dynamics (CFD), design of experiments (DoE), regression modeling, and multi-objective optimization to enhance ejector performance. A Box-Behnken design explores five key geometrical parameters, while a quadratic regression model establishes correlations between design variables and performance. Two optimization techniques, Non-dominated Sorting Genetic Algorithm (NSGA-II) and Desirability Function (DF), are applied to maximize the entrainment ratio while maintaining choked flow conditions with Mach number specifically considered at the nozzle throat. Results identify nozzle throat diameter (NTD) and nozzle exit position (NXP) as most critical parameters governing ejector performance. The optimized ejector achieves a 20 % entrainment ratio improvement and enhanced performance across design and off-design conditions. Additionally, optimization suppresses shockwave formation, improving flow stability and recirculation efficiency. This study introduces a novel simulation-based optimization approach for PEMFC ejectors, providing a systematic methodology to improve efficiency and adaptability. The findings advance hydrogen fuel cell technology by improving fuel utilization and operational flexibility, enhancing ejectors viability for real-world applications.

1. Introduction

In recent years, hydrogen energy and fuel cell technology have gained increasing recognition for addressing critical global problems related to energy storage, environmental pollution, and the demanding goal of attaining net zero emissions [1,2]. Hydrogen is highly attractive in terms of flexibility as an eco-friendly vector of energy as the world gradually moves towards newer and cleaner systems of energy conversion [3]. Fuel cells, especially proton exchange membrane fuel cells (PEMFC), have proved very efficient in converting hydrogen into electrical energy with only water as a by-product, therefore giving a clear opportunity to seriously reduce greenhouse gas emissions [4]. This advanced technology aligns with the growing demand for renewable energy sources and presents a carbon-neutral outlook for the future of cleaner transportation systems, electricity generation, and energy storage applications [5,6].

A crucial aspect of PEMFC operation is hydrogen recirculation, which ensures efficient fuel utilization and longevity of the fuel cell

* Corresponding author.
E-mail address: domenico.ferrero@polito.it (D. Ferrero).

https://doi.org/10.1016/j.jpowsour.2025.236846
Received 28 January 2025; Received in revised form 16 March 2025; Accepted 18 March 2025
Available online 26 March 2025
0378-7753/© 2025 The Authors. Published by Elsevier B.V. This is an open access article under the CC BY-NC-ND license (http://creativecommons.org/licenses/by-nc-nd/4.0/).

stack [7]. Since hydrogen is an expensive fuel, excess hydrogen must be recycled and fed back into the fuel cell to increase its utilization and efficiency. Various hydrogen recirculation methods exist, including mechanical pumps, ejectors, and electrochemical pumps, each offering distinct advantages [8]. Amongst these, ejectors are significant due to their simple design, low cost, and zero energy consumption in operation [9]. These benefits have led to their application in fields such as seawater desalination, aerospace, refrigeration, automotive industries, and solid oxide fuel cells [10–13].

An ejector is a device designed to mix two fluid streams through two inlets leading to a single output [14]. Its operation involves promoting supersonic flow, using components such as nozzle, suction chamber, mixing chamber, and diffusion chamber. The performance of an ejector is influenced by parameters like chamber dimensions, fluid properties, and operating conditions. The entrainment ratio, defined as the ratio of the secondary fluid's mass flow rate to the primary fluid's mass flow rate, is a key performance metric [15].

While ejectors offer significant advantages, their performance is highly dependent on operating conditions. When designed with fixed geometric parameters, they achieve optimal performance only under specific conditions. Operating outside these conditions results in reduced efficiency, backflow of the secondary stream, and even local hydrogen starvation, which can negatively impact the fuel cell's longevity. Various studies have attempted to optimize ejector performance through different approaches. For example, Zou et al. [16] tried to optimize the ejector used for heat pump system of an electric vehicle by means of genetic algorithm, ultimately observing improvements in overall performance of system under both heating and cooling conditions. Zhang et al. [17] proposed a multi-objective optimization method based on genetic algorithms in order to optimize the nozzle geometry of a steam ejector. The results represented an increase of around 27 % in entrainment ratio compared with the initial design. Shukla et al. [18] optimized some geometrical parameters of a refrigeration ejector such as nozzle throat diameter, mixing chamber, and diffuser length using neural network and genetic algorithm and they have found improvement in terms of entrainment ratio observing only a 3.67 % difference between the predicted and simulation results. Li et al. [19] focused on optimizing the geometric parameters of a carbon capture system's condensation ejector. They individually adjusted the length and diameter of the mixing chamber, as well as the distance from the nozzle exit to the mixing chamber inlet. Their sensitivity analysis showed that the diameter of the mixing chamber had the most significant effect on the entrainment ratio.

The integration of ejectors into PEMFC systems has gained interest, but challenges remain in ensuring efficiency across varying operating conditions. To address these challenges, researchers have explored structural modifications, including parallel ejectors, multi-nozzle ejectors, bypass ejectors, and variable ejectors. However, these solutions increase system complexity and manufacturing costs. Instead, optimizing the geometric parameters of a single-nozzle ejector which can cover a wider operational range, remains a key focus. To this end, Bai et al. [20] optimized key geometric parameters of the ejector, such as mixing chamber length, diffuser length, nozzle exit position, and diffuser outlet diameter, using a hybrid artificial fish swarm algorithm. Their optimized ejector achieved a higher entrainment ratio in wider operational range, compared to the design optimized by Maghsoodi et al. [21]. Similarly, Shen et al. [22] conducted orthogonal experiments combined with single-factor analysis to investigate the effects of critical parameters, including nozzle throat diameter, nozzle exit position, nozzle opening angle, and mixing chamber diameter, on the performance of the ejector in the PEMFC anodic recirculation system.

While some researchers have proposed modifying the ejector structure with new geometric configurations, such as parallel ejectors, multi-nozzle ejectors, bypass ejectors, variable ejectors, and combining blowers with ejectors in parallel, to extend the operational range [23–28], others argue that such approaches increase system complexity and raise manufacturing and control costs [29]. As a result, developing an optimal single-nozzle ejector capable of operating over an expanded range remains a key focus. In pursuit of this, Ma et al. [30] conducted a 2D computational fluid dynamics (CFD) analysis along with sensitivity analysis on various ejector geometries to evaluate the impact of parameters such as nozzle throat diameter, nozzle exit position, mixing chamber and secondary inlet diameters. Their results demonstrated that optimizing these parameters for a single-nozzle ejector can significantly extend the operational range. Additionally, Hou et al. [31] implemented a multi-objective optimization by weighting the entrainment ratio for both low and high operational conditions. They also performed experimental tests to validate their findings, which proved effective in enhancing the entrainment ratio and covering a broader range of PEMFC operating conditions.

The Box-Behnken Design (BBD) is an efficient response surface methodology used to develop quadratic models while minimizing computational and experimental costs. By strategically selecting midpoints and avoiding extreme points, BBD effectively captures both linear and interaction effects, making it well-suited for optimizing ejector performance [32]. In this study, a linear regression analysis was performed using a dataset of 46 geometric configurations of the ejector, generated through a Design of Experiments (DoE) approach based on BBD, and simulated using a 3D CFD model. The focus was on optimizing five key geometrical parameters namely Nozzle throat diameter (*NTD*), Nozzle exit position (*NXP*), Mixing chamber length (*MCL*), Diffuser length (*DL*), and Diffuser divergent angle (*DDA*), with Mach number (*Ma*) and entrainment ratio (ω) as the response variables. The BBD design was chosen due to its ability to efficiently construct quadratic polynomial models, enabling analysis of both individual and interaction effects among the ejector's geometric parameters. This approach helped identify significant parameter interactions influencing ejector performance. Additionally, statistical graphical tools, such as main effect plots and Pareto charts, were used to illustrate the impact of each parameter. Two multi-objective optimization algorithms, the Non-dominated Sorting Genetic Algorithm (NSGA-II) and Desirability Function (DF), were applied to optimize the ejector's geometry, aiming to maximize the entrainment ratio while maintaining choked flow conditions across both design and off-design operations.

2. Materials and methods

The framework implemented in this study is illustrated in Fig. 1. This research established the CFD modeling of an ejector suitable for a 100 kW PEMFC stack, a typical size for automotive applications. The model considers several geometrical parameters, including nozzle throat diameter, nozzle exit position, mixing chamber length, diffuser length, and diffuser divergent angle, to prepare a dataset according to the DoE method i.e. Box-Behnken design. Furthermore, the designed geometric configurations were numerically simulated using the model to obtain the magnitudes of the entrainment ratio and Mach number as the two main performance indicators for the ejector. The results were then analyzed using statistical approaches to determine how the ejector's geometric parameters affect its performance. Subsequently, the DF and NSGA-II optimization algorithms were applied to optimize the ejector geometry to increase the entrainment ratio while keeping the ejector in the choked region. Finally, the values of the ω and *Ma* for the optimum ejector geometry, as predicted by the aforementioned optimization algorithms, were evaluated using numerical modeling.

2.1. Ejector principle and design

Fig. 2(a) illustrates an ejector-based hydrogen recirculation system, which includes a hydrogen cylinder, pressure regulator valve, ejector, proton exchange membrane fuel cell (PEMFC), gas-water separator, and purge valve. The ejector recirculates unutilized hydrogen from the anode outlet of the PEMFC system through the secondary inlet. The

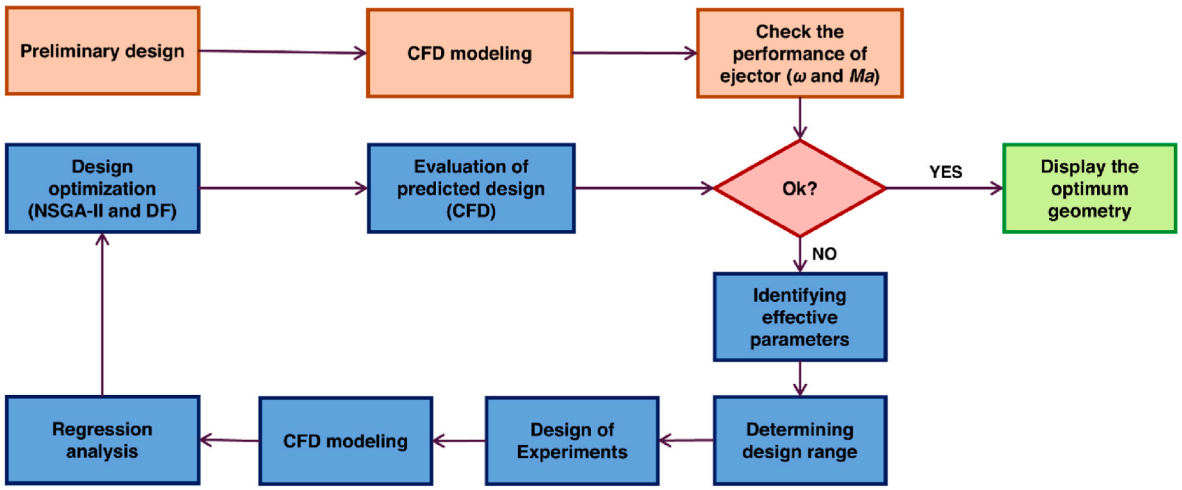


Fig. 1. A schematic representation of the method employed in this work, which is a combination of CFD, design of experiments (DoE), regression analysis, and multi-objective optimization.

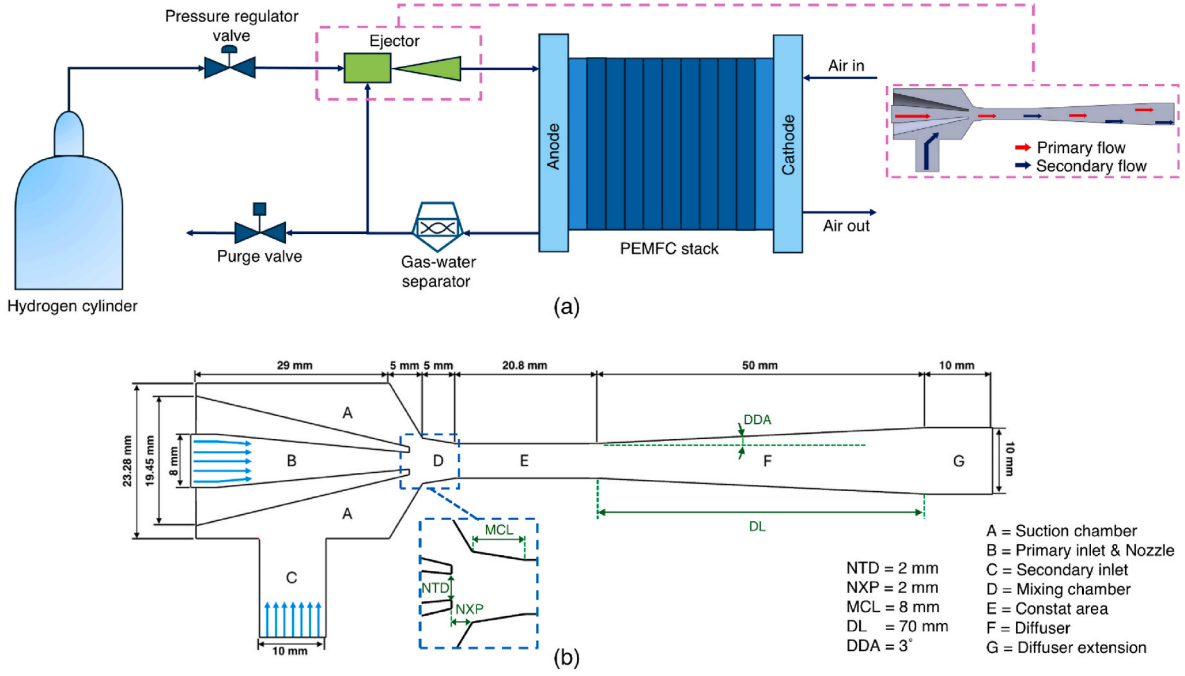


Fig. 2. Representation of: (a) schematic diagram of an ejector-based hydrogen supply system for a PEM fuel cell, and (b) schematic diagram of initial ejector geometry together with its various sections and dimensions.

performance of the ejector is influenced by the PEMFC operating conditions, particularly variations in hydrogen supply pressure. While the ejector operates efficiently at lower power outputs, its effectiveness may decline at higher power outputs due to increased energy losses associated with elevated hydrogen supply pressure.

Fig. 2(b) provides a detailed schematic of the ejector, highlighting its key geometrical parameters such as *NTD*, *NXP*, *MCL*, *DL*, and *DDA*. These parameters play a crucial role in the ejector's performance and are fundamental to its design. The ω is commonly used to evaluate the ejector's performance in the PEMFC system, expressed as:

$$\omega = \frac{\dot{m}_s}{\dot{m}_p} \tag{1}$$

where $\dot{m}_s$ denotes the mass flow rate of the secondary gas coming from the anode outlet, and $\dot{m}_p$ is the mass flow rate of the primary gas entering the primary nozzle of the ejector.

The *NTD* is one of the most critical dimensions in ejector design [33], as it directly influences the hydrogen flow rate and entrainment performance. It is determined based on the maximum fuel consumption rate and the maximum pressure of the primary flow, assuming critical flow conditions and ideal gas behavior. The *NTD* is calculated as follows [34]:

$$\dot{n}_{p,in} \times M_{w,p} = \mathrm{C} \times \pi \left(\frac{D_{nt}}{2}\right)^2 \times P_{p,in} \times 10^5 \times \sqrt{\gamma \times \frac{M_{w,p}}{R \times (T_{p,in} + 273.15)} \times \left(\frac{2}{\gamma+1}\right)^{\frac{\gamma+1}{\gamma-1}}} \tag{2}$$

where the fuel consumption rate depends on the stack current and number of cells of stack as below:

$$\dot{n}_{p,in} = \frac{N_{cell} \times I}{2 \times F} \tag{3}$$

All the parameters used in equations (2) and (3) are listed in Table 1 and the rest of geometries shown in Fig. 2(b) are considered based on the experimental study conducted by Xue et al. [24] who designed ejectors for a wide range of PEMFC stack sizes up to 100 kW, ensuring compatibility with our system. This selection ensures that the ejector operates efficiently under various hydrogen flow conditions and prevents backflow or choking.

2.2. Numerical modeling

2.2.1. Governing equations

To conduct the numerical simulations, several assumptions were made. Firstly, the fluid inside the ejector is considered to be pure hydrogen and compressible under steady-state conditions. Moreover, the fluid is assumed to behave as an ideal gas, with the effects of gravity being ignored. Since the simulation is performed under steady-state conditions, only boundary conditions are required, and no initial conditions are needed. Furthermore, the inner wall of the ejector is regarded as adiabatic, and phase changes are neglected, as they have been shown to have a negligible effect on the overall performance of the ejector [35]. Based on these assumptions, the governing equations utilized for numerical simulations are as follows:

The mass continuity equation:

$$\nabla.(\rho\vec{v}) = 0 \tag{4}$$

The momentum equations:

$$\nabla.\left(\rho\vec{v}_i\vec{v}_j\right) = -\nabla P + \nabla.\bar{\tau} + \rho\vec{g} \tag{5}$$

$$\bar{\tau} = \mu\left[\left(\nabla\vec{v} + \nabla\vec{v}^{T}\right) - \frac{2}{3}\nabla.\vec{v}I\right] \tag{6}$$

The energy conservation equation:

$$\nabla.[\vec{v}(\rho E + P)] = \nabla.\left(k_{eff}\nabla T - \sum h_j\vec{J}_j + \vec{v}\bar{\tau}\right) \tag{7}$$

The species transport equation:

$$\nabla.\left(\rho\vec{v}_i Y_q\right) = -\nabla.\vec{J}_q \tag{8}$$

Since the flow is compressible, density (ρ) varies with pressure and temperature, which is calculated using equation of state as below:

$$P = \rho RT \tag{9}$$

where in governing equations (equations (4)–(8)), i and j are the vectors' directions. ρ represents the fluid density, and v_i and v_j denote the velocity components. The term P refers to the pressure, while T is temperature, and R is the specific gas constant. The stress tensor is denoted by τ, and g represents the gravitational acceleration. The internal energy per unit mass is given by E, and h_j corresponds to the enthalpy. The species diffusion flux is represented by J_q, and k_{eff} denotes the effective thermal conductivity, which governs heat transport within the fluid.

Based on our previous literature review [36], the RNG k-ε is the most utilized turbulence model among others to study the fluid flow inside the ejectors used in PEMFC systems. Therefore, this model has been selected in order to assess the fluid turbulence in ejector using the following equations:

$$\frac{\partial}{\partial x_j}(\rho k v_i) + \rho\varepsilon + Y_M = \frac{\partial}{\partial x_j}\left(\alpha_k\mu_{eff}\frac{\partial k}{\partial x_j}\right) + G_k + G_b + S_k \tag{10}$$

$$\frac{\partial}{\partial x_j}(\rho\varepsilon v_i) + C_{2\varepsilon}\rho\frac{\varepsilon^2}{k} + R_\varepsilon = \frac{\partial}{\partial x_j}\left(\alpha_\varepsilon\mu_{eff}\frac{\partial\varepsilon}{\partial x_j}\right) + C_{1\varepsilon}\rho\frac{\varepsilon}{k}(G_k + C_{3\varepsilon}G_b) + S_\varepsilon \tag{11}$$

with

$$\mu_{eff} = \mu + \mu_t \tag{12}$$

$$\mu_t = \rho C_\mu\frac{k^2}{\varepsilon} \tag{13}$$

$$G_k = \mu_t\left(\frac{\partial v_i}{\partial x_j}\frac{\partial v_j}{\partial x_i}\right) \tag{14}$$

$$G_b = \beta g_i\frac{\mu_t}{Pr_t}\frac{\partial T}{\partial x_i} \tag{15}$$

$$Y_M = C_M\rho\frac{k}{a^2} \tag{16}$$

where in the turbulence model, the turbulent kinetic energy is denoted by k, while ε represents the turbulent dissipation rate, μ_{eff} is the effective viscosity, μ_t is the turbulent viscosity and, C_μ is the model constant. The terms G_k and G_b correspond to the production of turbulence due to mean velocity gradients and buoyancy, respectively. The compressibility effect is accounted for by Y_M, whereas S_k and S_ε represent source terms. The inverse turbulent Prandtl numbers for k and ε are given by α_k and α_ε, respectively. The empirical constants $C_{1\varepsilon}$, $C_{2\varepsilon}$, and $C_{3\varepsilon}$ influence the turbulence dissipation equation. Additionally, R_ε is an extra term that accounts for high-strain-rate effects, improving the accuracy of the turbulence model. T is the temperature, β is the thermal expansion coefficient, g_i is the gravitational acceleration, and Pr_t is the turbulent Prandtl number. Moreover, C_M is the model constant, and a is the speed of sound.

2.2.2. Boundary conditions

In this research, the ejector is tailored for a 100 kW PEMFC, with the ability to provide a maximum power of 101 kW and a minimum power of 8.5 kW based on study by Han et al. [27]. Therefore, the fuel cell stack's operating conditions are detailed in Table 2. The boundary conditions for the numerical simulation are established according to these operating conditions, as shown in Table 3. It is noteworthy to

Table 1
Parameters used in equations (2) and (3) to obtain nozzle throat diameter.

Parameter	Explanation	Value	Unit
$\dot{n}_{p,in}$	Max hydrogen consumption	0.7979	mol/s
$P_{p,in}$	Max primary inlet pressure	6	Bara
F	Faraday constant	96,485	C/mol
R	Universal gas constant	8.3145	J/(K mol)
Tp,in	Primary inlet temperature	20	°C
$M_{w,p}$	Molar weight	2.016×10^{-3}	kg/mol
γ	Isentropic expansion factor	1.4	–
C	Nozzle discharge coefficient	0.97	–
I	Current	240	A
N_{cell}	Number of cells	370	–

Table 2
The operating conditions of the ejector for a 100 kW PEMFC [27].

P_{stack} [kW]	V_{cell} [V]	$\dot{m}_p$ [kg/s]	P_{anode} [kPa]	T_{anode} [K]	ΔP_{anode} [kPa]
8	0.82	0.00011	133.3	331.2	3.1
17	0.80	0.00021	142.8	333.2	4.3
24	0.78	0.00032	152.2	335.2	5.4
31	0.76	0.00043	161.6	337.2	6.6
39	0.75	0.00054	171.1	339.2	7.7
53	0.73	0.00075	189.9	342.2	9.8
66	0.71	0.00097	208.7	346.2	11.2
78	0.69	0.00118	227.6	349.2	12.5
90	0.67	0.00140	246.5	350.2	13.8
101	0.65	0.00161	265.3	351.2	15.1

Table 3
The boundary conditions used for CFD simulations.

Boundary	Setting	Value
Primary inlet	Mass flow rate	$\dot{m}_p$ in Table 2 @ 298.2 K
Secondary inlet	Pressure	$P_s = P_{anode} - \Delta P_{anode}$ in Table 2
Outlet	Pressure	$P_{anode\ in}$ Table 2
Wall	No-slip and adiabatic	0 W/m^2

mention that in experimental studies, mass flow rate and pressure at the primary inlet are more commonly measured than velocity due to the feasibility of direct measurement. Therefore, specifying mass flow rate as a boundary condition aligns with real-world data availability. Additionally, the secondary inlet is defined using anode outlet pressure, which is typically measured in PEMFC systems.

2.2.3. Numerical solution

The simulations in this study were conducted in 3D using COMSOL Multiphysics 6.2, which employs the finite element method to discretize the model. The momentum, energy, and mass transport within the ejector were obtained using the MUMPS (MUltifrontal Massively Parallel sparse direct Solver) as the solver, whereas, the GMRES (Generalized Minimum RESidual) method was employed to solve the energy conservation equation. For each variable, a minimum convergence criterion of 10^{-6} was assumed.

2.2.4. Grid generation and grid independency

In this study, the built-in meshing tool of COMSOL Multiphysics 6.2 was used to mesh the ejector model with tetrahedral elements. The mesh size was further refined in critical regions using the adaptive mesh refinement method (Fig. 3(a)).

Moreover, to ensure the model's independence from the number of cells and to find the most appropriate grid size that balances computational cost and accuracy, Mach number and entrainment ratio were used as criteria to assess the stability of results tracking if there are any changes in their values with an increasing number of cells. The grid independence study indicated that refining beyond 391,336 cells resulted in less than a 1 % deviation in the normalized Mach number and entrainment ratio, as shown in Fig. 3(b); therefore, this grid size was used for further simulations.

2.3. Design of experiments (DoE) & regression analysis

The Box-Behnken Design (BBD) was used to obtain a set of ejector's configurations for five independent variables at three levels. The BBD was selected for this study due to its ability to efficiently explore the relationships between multiple variables while minimizing the number of combinations of variables required. Unlike full factorial designs, BBD reduces the number of high-cost simulations by avoiding combinations where all factors are at their extreme levels, yet it still provides comprehensive information about both the interactions and quadratic effects of the independent variables [37]. This makes BBD particularly well-suited for optimizing complex geometries like those of ejectors, as it balances design complexity with computational resource efficiency. The BBD uses the following formula in order to calculate the number of combinations [38]:

$$N = 2k(k-1) + C_0 \tag{17}$$

where k is number of independent variables and C_0 is the number of central points.

In this study, based on the design limitations, the design space has been determined (Table 4); Then, due to the fact that there are five independent variables and six central points, a numerical layout consisting of 46 combinations of parameters was generated as shown in Table 5.

After the completion of numerical simulations for all the combinations shown in Table 5, a regression model has been fitted to the dataset. The general form of a second-order polynomial regression model is as follows [39]:

$$Y = \beta_0 + \sum_{i=1}^{k} \beta_i X_i + \sum_{i=1}^{k} \beta_{ii} X_i^2 + \sum_{i=1}^{k} \sum_{i \neq j=1}^{k} \beta_{ij} X_i X_j + e \tag{18}$$

where Y denotes the response function i.e., ω and Ma in this study, X_i and X_j are the independent variables, β_0 is the constant coefficient, β_i, β_{ii}, and β_{ij} are the coefficients of linear, quadratic, and interaction terms, respectively, k is the number of independent variables which is equal to 5 in this study and e is the error.

Table 4
Design space including the studied independent variables and their levels.

Independent variables	Symbol	Level I	Level II	Level III
Nozzle throat diameter [mm]	NTD	1.5	2	2.5
Nozzle exit position [mm]	NXP	0	2	4
Mixing chamber length [mm]	MCL	5	8	11
Diffuser length [mm]	DL	50	70	90
Diffuser divergent angle [°]	DDA	1	3	5

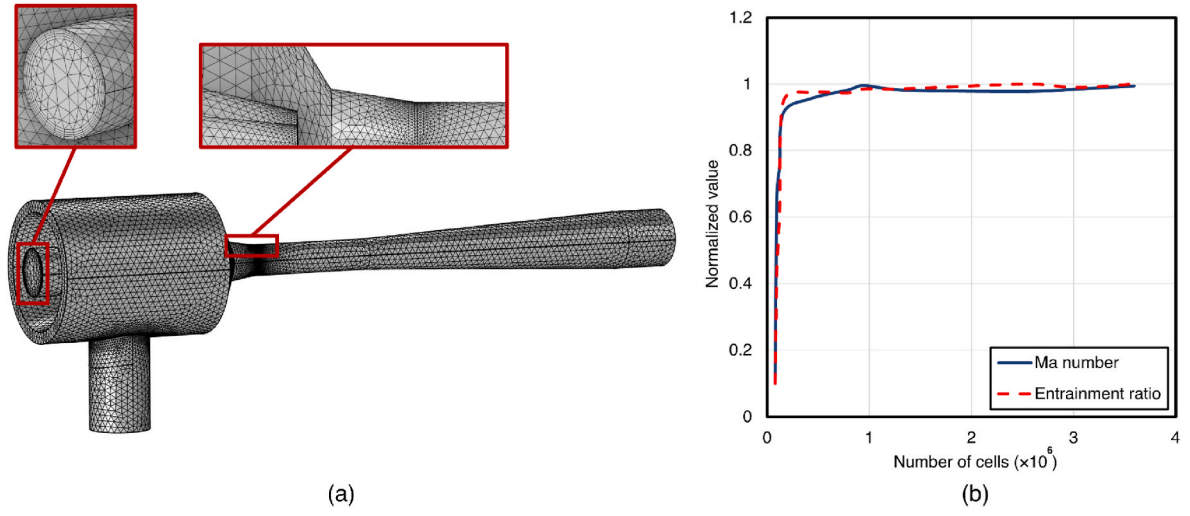


Fig. 3. Representation of (a) computational domain and grid structure of the ejector, and (b) grid independence study considering the magnitudes of both Ma and ω

Table 5
Geometric configurations layout provided by BBD, in which 46 CFD simulations were assigned, considering three levels for each independent variable.

Config. No.	NTD (mm)	NXP (mm)	MCL (mm)	DL (mm)	DDA (°)	Exp. No.	NTD (mm)	NXP (mm)	MCL (mm)	DL (mm)	DDA (°)
1	2	0	8	70	3	24	2	0	11	70	1
2	2	0	11	90	3	25	2	2	8	70	5
3	2	4	8	70	1	26	2	0	5	70	5
4	2	4	8	70	5	27	2	0	8	50	5
5	1.5	0	5	70	3	28	2	0	8	70	3
6	2	0	5	50	3	29	2	0	8	70	3
7	2	4	8	90	3	30	1.5	2	8	70	3
8	1.5	0	11	70	3	31	2.5	0	11	70	3
9	2	4	5	70	3	32	2.5	0	8	70	1
10	1.5	4	8	70	3	33	2	2	8	70	1
11	2.5	4	8	70	3	34	2	2	8	50	3
12	2.5	0	8	70	5	35	2.5	0	8	50	3
13	2	2	8	90	3	36	2	0	11	50	3
14	2.5	2	8	70	3	37	2	0	8	50	1
15	2	2	11	70	3	38	1.5	0	8	70	5
16	2	2	5	70	3	39	2	4	11	70	3
17	2	0	8	70	3	40	2	0	8	70	3
18	2	0	5	70	1	41	1.5	0	8	50	3
19	2	0	8	90	1	42	2	0	11	70	5
20	2	0	8	70	3	43	1.5	0	8	70	1
21	2.5	0	8	90	3	44	2.5	0	5	70	3
22	2	0	5	90	3	45	1.5	0	8	90	3
23	2	0	8	90	5	46	2	4	8	50	3

2.4. Multi-objective optimization

The optimization process, based on the fitted regression model, was performed using two different optimization methods: the non-dominated sorting genetic algorithm (NSGA-II) and the desirability function (DF) approach. These methods were applied to compare their effectiveness in optimizing ejector performance. Using two different methods allowed for cross-validation of the results, ensuring the reliability and robustness of the optimal solutions. The objective functions in both methods were identical, formulated as follows:

$$\max_{X} \left[\omega(X), -|Ma_{max}(X) - 1|\right] \tag{19}$$

with constraint of:

$$X_i^{min} \le X_i \le X_i^{max}, i = 1, 2, \ldots, 5 \tag{20}$$

where $\omega(X)$ is the entrainment ratio, modeled as a function of design variables, $Ma_{max}(X)$ is maximum Mach number, which is optimized to remain close to 1 by minimizing its absolute deviation, X_i represents the five design variables namely *NTD*, *NXP*, *MCL*, *DL*, and *DDA*, and X_i^{min} and X_i^{max} define the lower and upper levels, respectively, as reported in Table 4.

NSGA-II is an efficient multi-objective optimization algorithm that enhances the traditional genetic algorithm framework by incorporating non-dominated sorting and crowding distance mechanisms to maintain diversity among solutions [40]. It ranks the population on distinct fronts based on Pareto dominance, where a solution x dominates another solution y if it is at least as good in all objectives and strictly better in at least one. To preserve diversity, NSGA-II calculates the crowding distance d_i for each solution using the equation below [39]:

$$d_i = \sum_{j=1}^{M} \left(\frac{f_j^{i+1} - f_j^{i-1}}{f_j^{max} - f_j^{min}} \right) \tag{21}$$

where f_j^{i+1} and f_j^{i-1} are the neighboring objective values. The selection mechanism utilizes a crowded comparison operator based on rank and crowding distance to prioritize solutions. Crossover and mutation operators are employed to generate offspring, and elitism is used to combine parent and offspring populations, ensuring that the best solutions are retained for future generations.

The DF method is a statistical approach that converts multiple responses into a single composite score to aid decision-making. Each response is assigned a desirability value d_i between 0 (undesirable) and 1 (most desirable) based on its proximity to target values. The overall desirability is calculated by combining these individual scores, using the following equation [41]:

$$D = (d_1(Y_1) d_2(Y_2) \ldots d_\zeta(Y_\zeta))^{1/\zeta} \tag{22}$$

where, ζ represents the number of responses.

3. Results and discussion

3.1. Experimental validation

In this study, the CFD model is validated using results from two experimental studies. The first study conducted by Hou et al. [31] is used to validated the entrainment ratio as the global performance criteria, while the second study carried out by Sriveerakul et al. [42] is employed in order to validate the wall pressure as the local performance of ejector with an uncertainty of ±0.25 %. The experimental ejector models in these studies feature a single-nozzle configuration with an identical primary nozzle configuration, which is comparable to the geometry used in our numerical simulations. Moreover, the relative error (*Err*) is defined in order to compare the results of CFD analysis to those of experiments based on the following equation:

$$Err = \left| \frac{X_{CFD} - X_{EXP}}{X_{EXP}} \right| \tag{23}$$

where X_{CFD} and X_{EXP} stand for CFD numerical, and experimental-based magnitudes of global performance parameters, respectively.

Table 6
Comparing the results of numerical simulations and experimental tests [31].

$\dot{m}_p$ [kg/s]	P_{anode} [kPa]	P_s [kPa]	ω_{CFD} [−]	ω_{EXP} [−]	*Err* [%]
0.000149	130.00	128.45	1.20	1.14	5.26
0.000297	140.00	135.23	1.53	1.49	2.68
0.000446	150.00	140.97	1.71	1.67	2.39
0.000595	160.00	148.06	1.62	1.54	5.19
0.000744	180.00	164.35	1.41	1.59	11.32
0.000892	190.00	171.34	1.65	1.51	9.27
0.001041	210.00	188.80	1.40	1.47	4.76
0.001339	230.00	201.80	1.41	1.40	0.71

Table 6 compares the numerical and experimental global performance of the ejector. The maximum relative error in the entrainment ratio between the two approaches is 11.32 %, while the average deviation across all test cases is 5.2 %. These discrepancies could be attributed to manufacturing imperfections in the ejector and measurement inaccuracies, as noted by Hou et al. [31]. Additionally, numerical errors may arise due to assumptions in turbulence modeling, boundary conditions, and mesh resolution. While further refinement, such as adjusting the turbulence model or improving mesh quality, could potentially reduce this error, the overall agreement between the CFD and experimental results is strong.

Furthermore, Fig. 4 illustrates that the wall pressure distribution predicted by the CFD model aligns closely with the experimental data. The average relative error in wall static pressure across all measurement points is 6.5 %. The pressure distribution follows the expected trend within the ejector: a low-pressure region is observed after the primary nozzle due to the expansion of the high-velocity jet, followed by pressure fluctuations in the mixing section caused by turbulent interactions between the primary and secondary flows. As the flow progresses into the diffuser, the pressure gradually increases due to subsonic diffusion, enabling efficient pressure recovery. It is important to note that the boundary conditions used for this validation were chosen based on the experimental study to ensure consistency and enhance the reliability of the comparison. Overall, these results confirm that the CFD model effectively predicts the performance of the ejector.

3.2. Results of simulations on BBD matrix

CFD simulations are conducted based on the 46 geometric configurations created by Box-Behnken design (BBD). Subsequently, the magnitudes of responses (i.e., entrainment ratio and *Ma* number) were evaluated for each configuration and can be found in Table 7.

3.3. Statistical analysis

The regression equations incorporated all linear, quadratic, and interaction terms. To evaluate the model's fit, key assumptions were examined, including case independence, normal distribution, and consistent variance across predictions (homoscedasticity) [43]. The backward elimination method was employed to discard insignificant terms. Nevertheless, due to the hierarchical nature of the model, certain lower-order terms, even if not statistically significant, were retained. In addition, the significance of the terms in the fitted model was confirmed based on their probability at a 95 % confidence level. Moreover, a 10-fold cross-validation was performed to assess the model's robustness and generalizability, ensuring reliable performance across different data subsets. Statistical analyses were conducted using Minitab® Statistical Software (version 21, Minitab, LLC, State College, PA, USA).

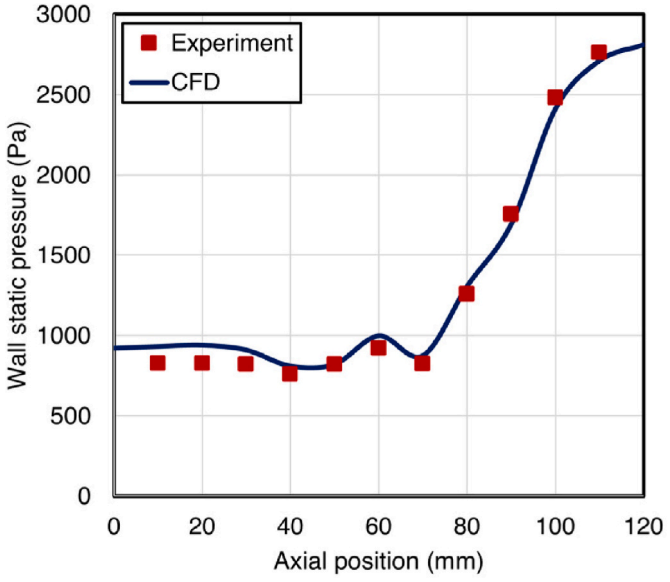


Fig. 4. Comparison between numerical and experimental wall static pressure (P_p = 270.28 kPa, T_p = 130 °C, P_s = 1.228 kPa, Ts = 10 °C, P_{anode} = 3.00 kPa) [42].

Table 7
Results of CFD simulation of 46 configurations created by BBD.

Config. No.	ω	*Ma*	Config. No.	ω	*Ma*
1	1.84	1.4	24	1.86	1.4
2	1.85	1.38	25	1.79	1.38
3	1.85	1.36	26	1.66	1.4
4	1.78	1.3	27	1.76	1.4
5	1.88	1.81	28	1.76	1.4
6	1.76	1.42	29	1.76	1.4
7	1.75	1.4	30	1.97	1.7
8	1.96	1.78	31	1.66	0.90
9	1.85	1.35	32	1.61	0.93
10	1.95	1.73	33	1.85	1.36
11	1.66	0.88	34	1.85	1.36
12	1.50	0.91	35	1.63	0.95
13	1.86	1.35	36	1.85	1.35
14	1.54	0.91	37	1.84	1.4
15	1.84	1.32	38	1.91	1.8
16	1.86	1.35	39	1.83	1.35
17	1.83	1.4	40	1.83	1.4
18	1.78	1.41	41	1.95	1.76
19	1.84	1.4	42	1.85	1.4
20	1.84	1.4	43	1.95	1.8
21	1.65	0.95	44	1.55	1
22	1.77	1.41	45	1.95	1.8
23	1.76	1.4	46	1.83	1.35

The 2nd order polynomial equations that were assigned to the responses (i.e., ω, and *Ma*) are expressed in Equations (16) and (17), respectively. Moreover, the details of ANOVA results for ω and *Ma* are presented in Tables 8 and 9, respectively.

$$\omega = 1.837 + 0.278NTD + 0.077NXP + 0.0031MCL - 0.0189DDA - 0.1514NTD^2 - 0.0058NXP^2 - 0.0056DDA^2 - 0.0061NXP \times MCL + 0.0046MCL \times DDA \quad (24)$$

$$Ma = 2.542 - 0.253NTD - 0.037NXP - 0.0056MCL - 0.147NTD^2 + 0.0061NXP^2 - 0.012NTD \quad (25)$$

The regression models for ω and *Ma* demonstrate strong predictive accuracy based on the ANOVA results (Tables 8 and 9). For ω, key

Table 8
Results of ANOVA for ω, together with coefficient of determination.

Source	DF	Adj. SS	Adj. MS	*F*-value	*p*-value
Regression	9	0.5177	0.0575	105.20	0.000
NTD	1	0.0029	0.0029	5.41	0.026
NXP	1	0.0157	0.0157	28.72	0.000
MCL	1	0.0001	0.0001	0.24	0.625
DDA	1	0.0005	0.0005	0.95	0.335
NTD^2	1	0.0141	0.0141	25.90	0.000
NXP^2	1	0.0032	0.0032	5.96	0.020
DDA^2	1	0.0055	0.0055	10.14	0.003
NXP × MCL	1	0.0102	0.0102	18.67	0.000
MCL × DDA	1	0.0030	0.0030	5.53	0.024
Error	36	0.0196	0.0007		
Total	45	0.5373			
S	R^2 (%)	R^2_{adj} (%)	R^2_{pred} (%)	10-fold S	10-fold R^2 (%)
0.0233	96.34 %	95.42 %	94.12 %	0.0284	93.08 %

Table 9
Results of ANOVA for *Ma*, together with coefficient of determination.

Source	DF	Adj. SS	Adj. MS	*F*-value	*p*-value
Regression	5	2.8869	0.5773	1432.35	0.000
NTD	1	0.0025	0.0025	6.27	0.016
NXP	1	0.0089	0.0089	22.11	0.000
MCL	1	0.0045	0.0045	11.30	0.002
NTD^2	1	0.0139	0.0138	34.48	0.000
NXP^2	1	0.0035	0.0035	8.79	0.005
Error	40	0.0161	0.0004		
Total	45	2.9031			
S	R^2 (%)	R^2_{adj} (%)	R^2_{pred} (%)	10-fold S	10-fold R^2 (%)
0.02	99.44	99.38	99.22	0.0225	99.20

parameters such as *NXP*, NTD^2, and *NXP* × *MCL* exhibit an extremely significant effect ($p < 0.01$), while *NTD*, NXP^2, DDA^2, *NXP* × *MCL*, and *MCL* × *DDA* show a significant effect ($p < 0.05$). Similarly, for *Ma*, the factors *NXP*, NTD^2, and NXP^2 are highly significant ($p < 0.01$), confirming their strong influence on the response. The high R^2 values indicate that both models fit the data well, with R^2 exceeding 96 % for ω and 99 % for *Ma*, demonstrating their strong explanatory power.

To assess potential overfitting, 10-fold cross-validation R^2 values were computed, yielding 93.08 % for ω and 99.20 % for *Ma* confirming that the models generalize well to unseen data. Additionally, stepwise regression with hierarchical constraints was applied to retain only statistically justified terms, ensuring both interpretability and model stability while minimizing unnecessary complexity.

The Pareto chart displays the absolute values of the normalized effects, ranging from the largest to the smallest, enabling the assessment of both the magnitude and significance of each effect. In these plots, bars that extend beyond the reference line indicate statistically significant effects.

As can be seen in Fig. 5(a, and b), for the ω, the most influential factors include *NXP*, NTD^2, and the interaction between *NXP* and *MCL*, while other terms such as DDA^2, and NXP^2 also contribute significantly. In contrast, the *Ma* is primarily influenced by NTD^2, followed by *NXP*, and NXP^2. The results indicate that *NTD* and *NXP*, along with their squared are critical parameters for both responses, underscoring their importance in optimizing the model's performance. Although the Pareto chart helps compare the importance of each independent variable, the main effect plot is helpful in visualizing how changes in individual independent variable impact the response variable. Fig. 5(c) demonstrates that *NTD* has the most significant negative effect on ω, as increasing *NTD* leads to a notable reduction. Similarly, *NXP* exhibits a non-linear effect, while *MCL* positively influences ω as its value increases. Both *DL* and *DDA* have minor impacts on this response. In contrast, Fig. 5(d) reveals that *Ma* is also highly sensitive to *NTD*, which exerts a strong negative effect. The impact of *NXP* is significant initially but levels off at higher values. In contrast, *MCL*, *DL*, and *DDA* have little to no effect on *Ma*. These findings are consistent with respect to those of pareto charts, highlighting the importance of optimizing *NTD* and *NXP*.

3.4. Optimization

The ANOVA results clarified the effectiveness and importance of each independent variable. Furthermore, it was demonstrated that to achieve a higher entrainment ratio while maintaining the ejector in a choked condition, an optimization process can be conducted to determine the optimal ejector configuration. To achieve this, two optimization algorithms, namely NSGA-II, developed by scripting in Python and DF, acquired by Minitab® Statistical Software, were employed with the objective of maximizing the entrainment ratio while ensuring the ejector does not enter the supersonic regime. The predicted optimal designs were ultimately verified through CFD analysis to assess the extent of deviation from the predicted design results.

Fig. 6 presents a comparison of the ω magnitude between the initial design and the optimized design, alongside the verification of the

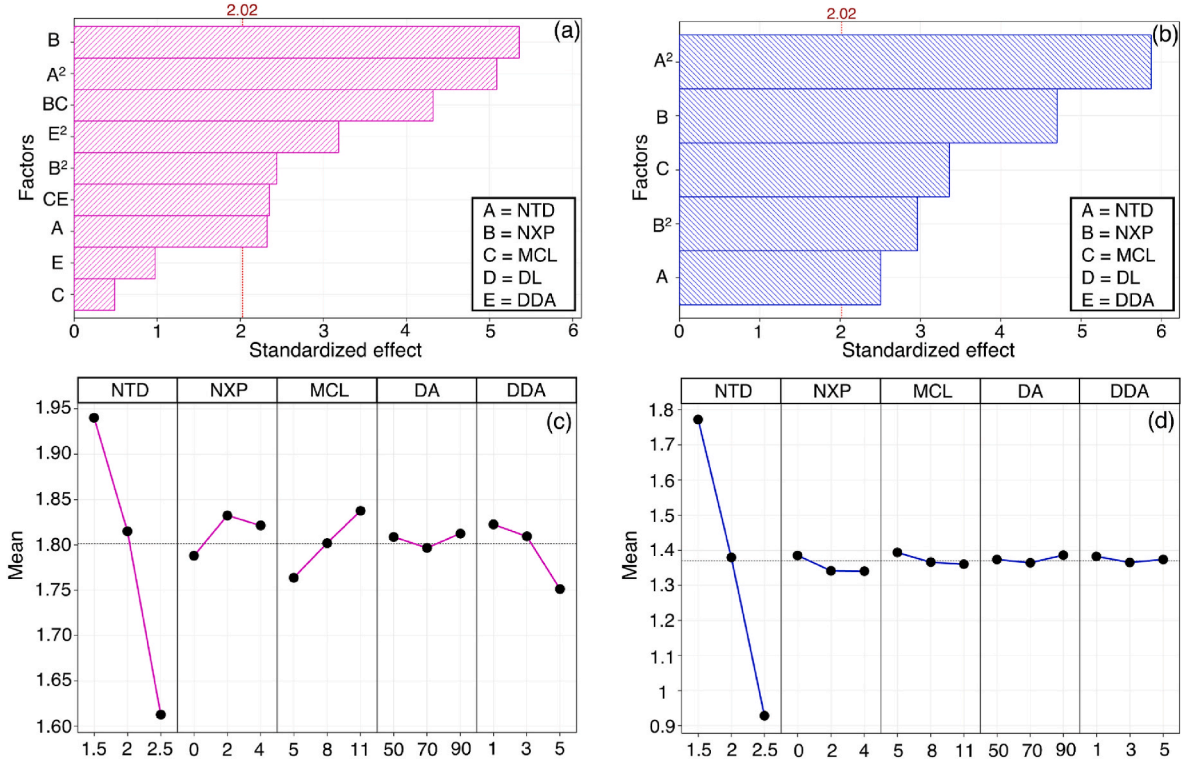


Fig. 5. The Pareto chart of standardized effects at a significance level of $\alpha = 0.05$ illustrates the impact of the linear, quadratic, and interaction forms of independent variables on the responses studied: (a) ω, and (b) *Ma*, and main effects plots, which show how each independent variable affects the response variable: (c) ω, and (d) *Ma*.

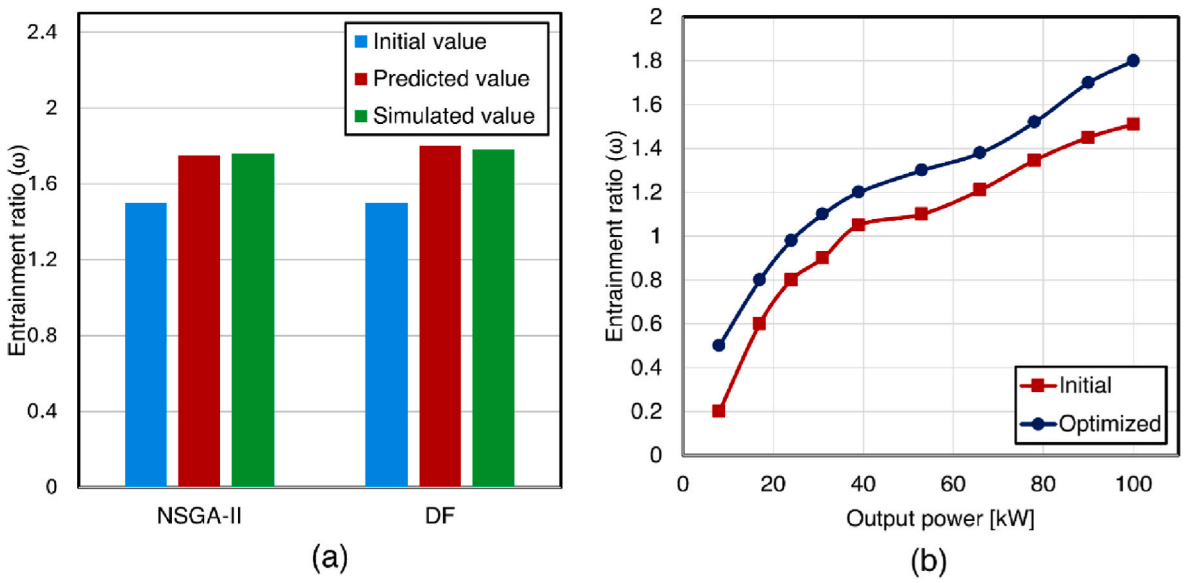


Fig. 6. (a) Comparison of the ω obtained for the initial geometry, the predictions from both NSGA-II and DF algorithms, and the simulation results for the optimized geometry, (b) performance of both initial and optimized (by NSGA-II) ejector in off-design conditions.

optimized design using CFD analysis for both optimization algorithms. As can be seen in Fig. 6(a), both methods show a significant improvement in the entrainment ratio. The entrainment ratio increased by approximately 20 % for both methods, which is a substantial improvement from the initial design. Moreover, it can be observed that the overall performance of ejector in off-design conditions has been significantly improved.

To further evaluate the impact of the optimization process on ejector performance, the *Ma* and wall static pressure distributions along the ejector centerline for both the optimized design and selected

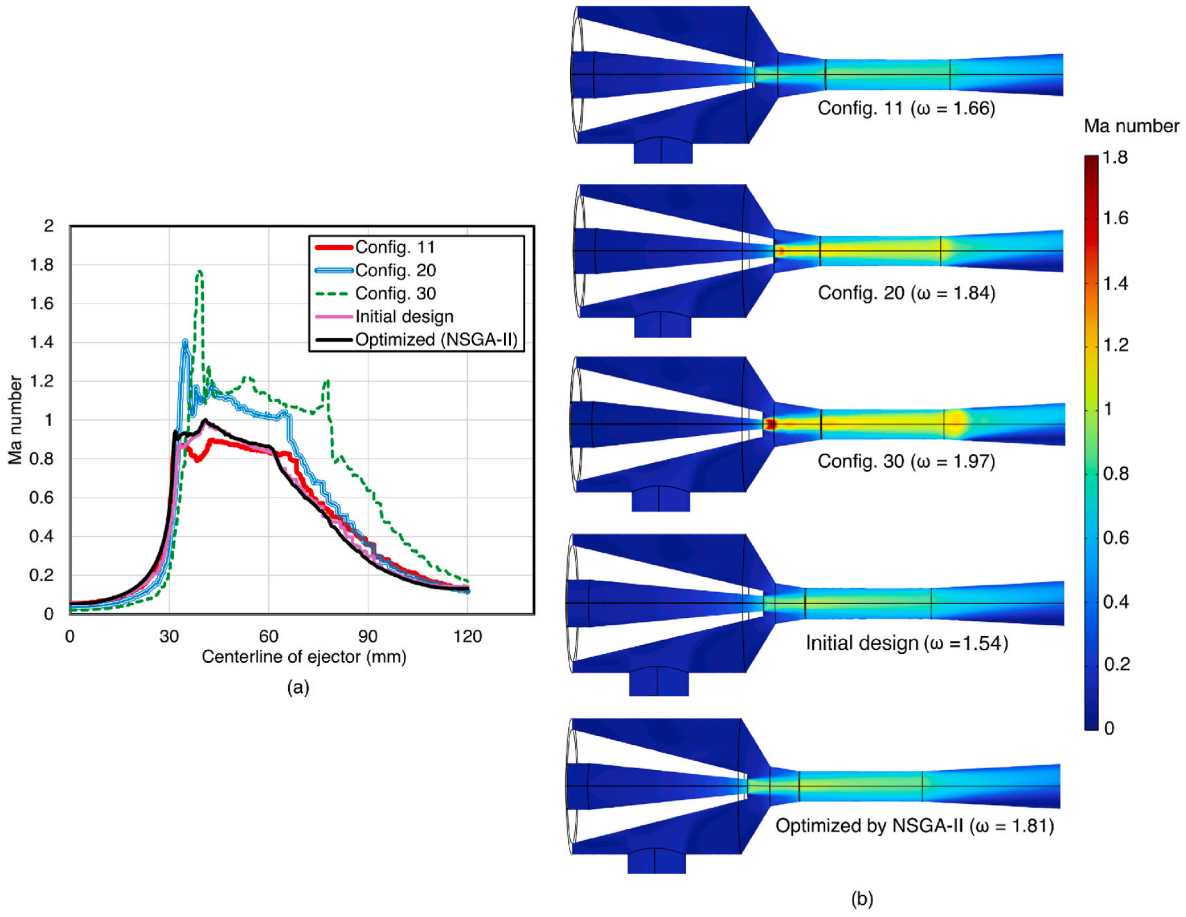


Fig. 7. Representation of, (a) the *Ma* magnitude along the centerline of ejector for optimized (by NSGA-II) and three other configurations, and (b) distribution of *Ma* in different ejector configurations.

configurations (i.e., configuration numbers 11, 20, and 30, as represented in Table 5) were analyzed. The *Ma* distribution along the ejector centerline, as shown in Fig. 7, highlights the performance differences between the optimized design and the configurations. The optimized profile (black line) exhibits a smooth and controlled *Ma* increase, peaking just below 1, indicative of subsonic flow throughout the ejector. This behavior is attributed to the optimized geometrical parameters of ejector, which promote gradual acceleration of the primary flow and more effective mixing with the secondary flow. By ensuring controlled expansion, the optimized design minimizes adverse pressure gradients, reducing the likelihood of shockwave formation and flow separation. Additionally, the gradual increase in *Ma* reflects efficient momentum exchange between the primary and secondary streams, preventing sudden velocity mismatches that could induce flow instabilities.

Maintaining the peak *Ma* just below 1 suggests that the ejector operates in a choked flow condition, where the flow reaches the maximum allowable velocity without transitioning to supersonic speeds. This condition prevents the formation of strong normal shocks, which would otherwise cause abrupt pressure drops and energy dissipation. In contrast, the geometric configurations investigated, particularly configuration 30 (green dashed line), reach a peak *Ma* of approximately 1.8, indicating the presence of strong shocks that disrupt flow continuity. This is due to the inadequate control of flow expansion, leading to excessive acceleration and subsequent deceleration through shock interactions. These results are consistent with previous studies [44,45], which have demonstrated that such supersonic conditions can lead to significant energy losses, inefficiencies in hydrogen recirculation, and potential flow destabilization.

The static pressure distribution in the ejector, as illustrated in Fig. 8, further emphasizes the performance differences between the optimized design and the configurations investigated. The optimized profile demonstrates a gradual and consistent pressure drop along the ejector centerline (see Fig. 8(a)), reflecting smoother pressure recovery and better momentum transfer. This steady pressure reduction indicates efficient flow management, with minimal energy losses and fewer shock-induced disturbances. Similar findings were reported by Zhu et al. [46], who demonstrated that suppressing shock waves through geometric optimization improves pressure recovery and overall ejector performance. In contrast, Configuration 30 shows significant pressure fluctuations, particularly near the nozzle, where pressure spikes are indicative of strong shock waves. These sharp pressure changes can cause flow blockages, leading to inefficient mixing and reduced performance in hydrogen recirculation, consistent with the observations made by Li et al. [47]. The more abrupt and uneven pressure profile in Configuration 30 suggests poor flow control and energy dissipation, which contrasts with the optimized design's ability to maintain smoother pressure transitions. Zhu et al. [48] similarly observed that ejector designs optimized for pressure recovery exhibit reduced energy losses and better stability in flow management. The findings from this comparison highlight the critical role of optimizing geometric parameters like the *NTD* and *NXP* to achieve improved pressure recovery and overall ejector efficiency.

4. Conclusion

This study demonstrated the effectiveness of geometric optimization in enhancing the performance of hydrogen recirculation ejectors in PEMFC systems. By employing NSGA-II and the Desirability Function approach, the entrainment ratio improved by 20 %, leading to better hydrogen utilization and enhanced operational stability. The optimized

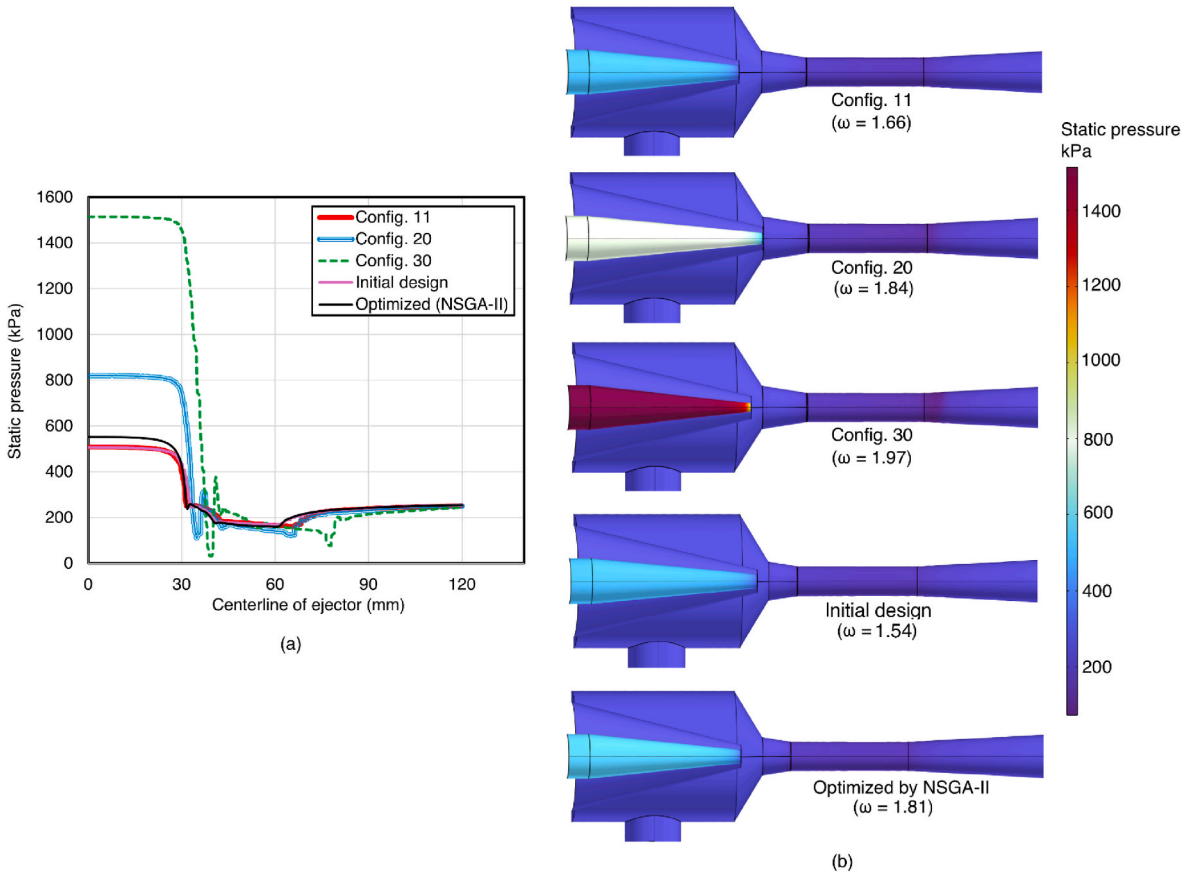


Fig. 8. Representation of, (a) the magnitude of static pressure along the centerline of ejector for optimized (by NSGA-II) and three other configurations, and (b) distribution of static pressure along the ejector wall for different ejector configurations.

ejector also maintained superior performance across a wider range of conditions, including off-design scenarios, reducing the risk of backflow and hydrogen starvation.

Despite these improvements, the study has some limitations. The optimization was performed under steady-state conditions, without accounting for transient effects or long-term degradation factors. Moreover, the numerical model was validated using experimental data from the literature rather than direct experimental testing of the optimized design.

Future work will focus on integrating the optimized ejector into a full PEMFC system model to assess its impact on fuel utilization efficiency and power output. Experimental validation will be conducted to evaluate hydrogen consumption and system efficiency changes. Additionally, transient and multi-phase flow conditions will be investigated, particularly the role of hydrogen recirculation in dynamic load responses and long-term stack performance. Comparative analysis of performance metrics such as voltage efficiency, polarization behavior, and degradation rates will further quantify the benefits of ejector optimization. Furthermore, adaptive control strategies will be explored to enhance ejector performance under varying operating conditions, improving the robustness and efficiency of PEMFC systems.

CRediT authorship contribution statement

Masoud Arabbeiki: Writing – original draft, Visualization, Validation, Software, Methodology, Formal analysis, Conceptualization. **Mohsen Mansourkiaei:** Writing – review & editing, Supervision, Resources, Methodology, Formal analysis, Conceptualization. **Domenico Ferrero:** Writing – review & editing, Supervision, Resources. **Massimo Santarelli:** Writing – review & editing, Supervision, Resources, Project administration, Funding acquisition.

Declaration of competing interest

The authors declare the following financial interests/personal relationships which may be considered as potential competing interests: Masoud Arabbeiki reports financial support was provided by Raicam Driveline Srl. If there are other authors, they declare that they have no known competing financial interests or personal relationships that could have appeared to influence the work reported in this paper.

Acknowledgments

The authors would like to acknowledge the support of Raicam Driveline S.r.l. for the development of this manuscript.

Data availability

The authors do not have permission to share data.

References

[1] D.T. Le Tri, et al., Optimization of the ejector parameters for anodic recirculation systems in high-performance dual-stack proton-exchange membrane fuel cells, Energy Convers. Manag. 296 (2023) 117712.
[2] B. Yin, et al., A novel dual-nozzle ejector for enhancement of hydrogen recirculation applied to proton exchange membrane fuel cell system, J. Power Sources 580 (2023) 233444.
[3] L. Chen, et al., Optimal design of a novel nested-nozzle ejector for PEMFC's hydrogen supply and recirculation system, Int. J. Hydrogen Energy 48 (70) (2023) 27330–27343.
[4] J.-K. Kuo, et al., Optimal technical analysis of vacuum ejector for passive hydrogen recovery, Int. J. Hydrogen Energy 48 (22) (2023) 8260–8272.
[5] G. Singer, et al., Ejector validation in proton exchange membrane fuel cells: a comparison of turbulence models in computational fluid dynamics (CFD) with experiment, Int. J. Hydrogen Energy 61 (2024) 1405–1416.
[6] Y. Huang, P. Jiang, Y. Zhu, Shape optimization and flow irreversibility mechanism analysis of normal temperature, high temperature and wet stream ejectors, Appl. Therm. Eng. 242 (2024) 122468.
[7] Z. Du, et al., Performance investigation on a coaxial-nozzle ejector for PEMFC hydrogen recirculation system, Int. J. Hydrogen Energy 46 (76) (2021) 38026–38039.
[8] P.-H. Huang, J.-K. Kuo, C.-B. Wu, Design and evaluation of dual passive hydrogen recovery subsystem for 10 kW PEMFC, Int. J. Hydrogen Energy 54 (2024) 483–490.
[9] Y. Liu, Z. Tu, S.H. Chan, Applications of ejectors in proton exchange membrane fuel cells: a review, Fuel Process. Technol. 214 (2021) 106683.
[10] Q. Yang, et al., Maximum thrust for the rocket-ejector mode of the hydrogen fueled rocket-based combined cycle engine, Int. J. Hydrogen Energy 40 (9) (2015) 3771–3776.
[11] H. Wu, et al., Numerical investigation of the influences of mixing chamber geometries on steam ejector performance, Desalination 353 (2014) 15–20.
[12] S. Tanaka, et al., Fuel cell system for Honda CLARITY fuel cell, ETransportation 3 (2020) 100046.
[13] S. Baba, et al., Development of anode gas recycle system using ejector for 1 kW solid oxide fuel cell, J. Eng. Gas Turbines Power 137 (2) (2015) 021504.
[14] L. Cai, M. He, A numerical study on the supersonic steam ejector use in steam turbine system, Math. Probl Eng. 2013 (1) (2013) 651483.
[15] W. Chen, et al., Numerical assessment of ejector performance enhancement by means of combined adjustable-geometry and bypass methods, Appl. Therm. Eng. 149 (2019) 950959.
[16] H. Zou, et al., Ejector optimization and performance analysis of electric vehicle CO2 heat pump with dual ejectors, Energy 239 (2022) 122452.
[17] G. Zhang, et al., Optimization of the primary nozzle based on a modified condensation model in a steam ejector, Appl. Therm. Eng. 171 (2020) 115090.
[18] P.B. Shukla, et al., Design optimization of ejectors using ANN and GA, in: Proceedings of the 26thNational and 4th International ISHMT-ASTFE Heat and Mass Transfer Conference December 17-20, 2021, IIT Madras, Chennai-600036, Tamil Nadu, India, Begel House Inc, 2021.
[19] R. Li, J. Yan, C. Reddick, Optimization of three key ejector geometries under fixed and varied operating conditions: a numerical study, Appl. Therm. Eng. 211 (2022) 118537.
[20] L.B. Reis, R. dos Santos Gioria, Optimization of liquid jet ejector geometry and its impact on flow fields, Appl. Therm. Eng. 194 (2021) 117132.
[21] A. Maghsoodi, E. Afshari, H. Ahmadikia, Optimization of geometric parameters for design a high-performance ejector in the proton exchange membrane fuel cell system using artificial neural network and genetic algorithm, Appl. Therm. Eng. 71 (1) (2014) 410–418.
[22] C. Shen, S. Xu, Design and characteristic analysis of ejector used in high-voltage proton exchange membrane fuel cell system, SAE Technical Paper (2020).
[23] E. Hosseinzadeh, et al., Numerical analysis of transport phenomena for designing of ejector in PEM forklift system, Int. J. Hydrogen Energy 39 (12) (2014) 6664–6674.
[24] H. Xue, et al., Design and investigation of multi-nozzle ejector for PEMFC hydrogen recirculation, Int. J. Hydrogen Energy 45 (28) (2020) 14500–14516.
[25] D.A. Brunner, et al., Design and characterization of an electronically controlled variable flow rate ejector for fuel cell applications, Int. J. Hydrogen Energy 37 (5) (2012) 4457–4466.
[26] J. He, J. Ahn, S.-Y. Choe, Analysis and control of a fuel delivery system considering a two-phase anode model of the polymer electrolyte membrane fuel cell stack, J. Power Sources 196 (10) (2011) 4655–4670.
[27] J. Han, et al., Performance investigation on the bypass ejector for a proton exchange membrane fuel cell system, Appl. Therm. Eng. 241 (2024) 122349.
[28] M. Yu, et al., Auxiliary-ejector-based hydrogen recirculation system to broaden PEMFC operating range, Int. J. Hydrogen Energy 57 (2024) 515–529.
[29] P. Pei, et al., Numerical studies on wide-operating-range ejector based on anodic pressure drop characteristics in proton exchange membrane fuel cell system, Appl. Energy 235 (2019) 729–738.
[30] T. Ma, et al., Numerical studies on ejector in proton exchange membrane fuel cell system with anodic gas state parameters as design boundary, Int. J. Hydrogen Energy 46 (78) (2021) 38841–38853.
[31] M. Hou, F. Chen, Y. Pei, Optimization of geometric parameters of ejector for fuel cell system based on multi-objective optimization method, Int. J. Green Energy 21 (2) (2024) 228–243.
[32] M.P. Iwundu, J. Cosmos, The efficiency of seven-variable box-behnken experimental design with varying center runs on full and reduced model types, J. Math. Stat. 18 (2022) 196–207.
[33] K. Nikiforow, et al., Designing a hydrogen gas ejector for 5 kW stationary PEMFC system–CFD-modeling and experimental validation, Int. J. Hydrogen Energy 41 (33) (2016) 14952–14970.
[34] D.W. Green, Perry's Chemical Engineers, handbook–seventh ed., Sections, 2008, pp. 5–12.
[35] J. Han, et al., Experimental and numerical study on the ejector containing condensable species in the secondary flow for PEM fuel cell applications, Appl. Therm. Eng. 232 (2023) 121091.
[36] M. Arabbeiki, et al., Ejectors in hydrogen recirculation for PEMFC-based systems: a comprehensive review of design, operation, and numerical simulations, Energies 17 (19) (2024) 4815.
[37] H. Ma, et al., Research on a new-designed Venturi ejector and dazomet particle motion characteristics for dilute-phase pneumatic conveying systems based on CFD-DEM, Comput. Electron. Agric. 213 (2023) 108240.
[38] S.C. Ferreira, et al., Box-Behnken design: an alternative for the optimization of analytical methods, Anal. Chim. Acta 597 (2) (2007) 179–186.

[39] A.A. Ahmadi, et al., Configuration and optimization of a minichannel using water–alumina nanofluid by non-dominated sorting genetic algorithm and response surface method, Nanomaterials 10 (5) (2020) 901.
[40] H. Fang, et al., An efficient non-dominated sorting method for evolutionary algorithms, Evol. Comput. 16 (3) (2008) 355–384.
[41] S. Kushwaha, et al., A modified desirability function approach for mean-variance optimization of multiple responses, Int. J. Software Sci. Comput. Intell. 5 (3) (2013) 7–21.
[42] T. Sriveerakul, S. Aphornratana, K. Chunnanond, Performance prediction of steam ejector using computational fluid dynamics: Part 1. Validation of the CFD results, Int. J. Therm. Sci. 46 (8) (2007) 812–822.
[43] R.N. Cardinal, M.R. Aitken, ANOVA for the Behavioral Sciences Researcher, Psychology Press, 2013.
[44] M. Hamzaoui, H. Nesreddine, Z. Aidoun, A numerical and experimental performance assessment of a single-phase supersonic ejector, Arabian J. Sci. Eng. 47 (7) (2022) 8899–8913.
[45] N. Bukharin, M. El Hassan, Numerical and experimental investigation of supersonic binary fluid ejector performance, Fluid 8 (7) (2023) 197.
[46] Y. Zhu, P. Jiang, Experimental and numerical investigation of the effect of shock wave characteristics on the ejector performance, Int. J. Refrig. 40 (2014) 31–42.
[47] Y. Li, et al., The effect of different pressure conditions on shock waves in a supersonic steam ejector, Energies 15 (8) (2022) 2903.
[48] Y. Zhu, P. Jiang, Experimental and analytical studies on the shock wave length in convergent and convergent–divergent nozzle ejectors, Energy Convers. Manag. 88 (2014) 907–914.